The Astrophysical Journal, 921:161 (13pp), 2021 November 10 https://doi.org/10.3847/1538-4357/ac1f20

Resolving the Fastest Ejecta from Binary Neutron Star Mergers: Implications for Electromagnetic Counterparts

Coleman Dean[1], Rodrigo Fernández[1], and Brian D. Metzger[2,3]
[1] Department of Physics, University of Alberta, Edmonton, AB T6G 2E1, Canada
[2] Department of Physics and Columbia Astrophysics Laboratory, Columbia University, Pupin Hall, New York, NY 10027, USA
[3] Center for Computational Astrophysics, Flatiron Institute, 162 5th Avenue, New York, NY 10010, USA
Received 2021 July 14; revised 2021 August 14; accepted 2021 August 17; published 2021 November 11

Abstract

We examine the effect of spatial resolution on initial mass ejection in grid-based hydrodynamic simulations of binary neutron star mergers. The subset of the dynamical ejecta with velocities greater than $\sim 0.6c$ can generate an ultraviolet precursor to the kilonova on approximately hour timescales and contribute to a years long nonthermal afterglow. Previous work has found differing amounts of this fast ejecta, by one to two orders of magnitude, when using particle-based or grid-based hydrodynamic methods. Here, we carry out a numerical experiment that models the merger as an axisymmetric collision in a corotating frame, accounting for Newtonian self-gravity, inertial forces, and gravitational wave losses. The lower computational cost allows us to reach spatial resolutions as high as 4 m, or $\sim 3 \times 10^{-4}$ of the stellar radius. We find that fast ejecta production converges to within 10% for a cell size of 20 m. This suggests that fast ejecta quantities found in existing grid-based merger simulations are unlikely to increase to the level needed to match particle-based results upon further resolution increases. The resulting neutron-powered precursors are in principle detectable out to distances $\lesssim$200 Mpc with upcoming facilities.We also find that head-on collisions at the freefall speed, relevant for eccentric mergers, yield fast and slow ejecta quantities of order $10^{-2}\,M_{\odot}$, with a kilonova signature distinct from that of quasi-circular mergers.

Unified Astronomy Thesaurus concepts: Gravitational waves (678); Hydrodynamics (1963); Neutron stars (1108); Nuclear astrophysics (1129); Shocks (2086); Transient sources (1851)

1. Introduction

Detection of electromagnetic (EM) emission from neutron star (NS) mergers provides additional information beyond that contained in the gravitational wave (GW) signal, as was demonstrated for GW 170817 (Abbott et al. 2017a). This information allows probing the merger environment (e.g., Blanchard et al. 2017; Levan et al. 2017), their use as standard sirens for cosmology (e.g., Abbott et al. 2017b), constraining their status as progenitors of short gamma-ray bursts (e.g., Abbott et al. 2017c), or assessing their contribution to the cosmic production of *r*-process elements (e.g., Cowperthwaite et al. 2017; Drout et al. 2017; Tanaka et al. 2017; Tanvir et al. 2017). Nucleosynthesis information is encoded in the kilonova signal, which arises from material ejected at subrelativistic speeds that is radioactively heated by freshly formed elements (Li & Paczyński 1998; Metzger et al. 2010).

The bulk of mass ejection in binary NS (BNS) mergers occurs in two ways. First, material is ejected on the dynamical time from the collision interface between the two stars or by tidal processes as the stars merge (e.g., Hotokezaka et al. 2013). Second, the accretion disk that forms after the merger ejects mass over longer timescales (see, e.g., Fernández & Metzger 2016 for a review). In both cases, the majority of the material is initially neutron-rich and moves at speeds $\lesssim 0.3c$, which allows the *r*-process to proceed to completion, with a composition pattern that depends on the level of reprocessing by neutrinos (e.g., Wanajo et al. 2014; Just et al. 2015; Martin et al. 2015; Wu et al. 2016; Lippuner et al. 2017; Roberts et al. 2017). This results in a kilonova signal that peaks in the optical or infrared band and which evolves on a day to week timescale (Kasen et al. 2013; Barnes & Kasen 2013; Tanaka & Hotokezaka 2013; Fontes et al. 2015).

If a fraction of the ejected material expands on sufficiently short timescales, a freeze out of the *r*-process can occur, with the ejecta consisting primarily of free, unprocessed neutrons that eventually undergo beta decay (Goriely et al. 2014). Freeze out of neutrons requires the density to drop to $\sim 4 \times 10^5$ g cm^{-3} on timescales shorter than $\sim$5 ms, which maps well to ejecta with velocities $\gtrsim 0.6c$ (Metzger et al. 2015). Such ejecta can also generate EM emission (Kulkarni 2005), and if launched ahead of slower material, can provide an ultraviolet *precursor* to the kilonova that evolves on a timescale of hours after the merger (Metzger et al. 2015). Detection of EM emission on a timescale of hours could have differentiated among various models that account for the kilonova from GW 170817, but which diverge before the earliest EM observation at $\sim$11 hr post-merger (Arcavi 2018).

The existence of sufficient ejecta with the required speed to generate a detectable neutron-powered precursor is not clear, however. A fast component with mass $\sim 10^{-4}\,M_{\odot}$ was first obtained in smoothed particle hydrodynamic (SPH) simulations of BNS mergers (Bauswein et al. 2013), but grid-based hydrodynamic simulations have found much smaller quantities ($\sim 10^{-7}$–$10^{-5} M_{\odot}$, e.g., Ishii et al. 2018; Radice et al. 2018), making a potential kilonova precursor much harder to detect given the expected distance to most sources ($\gtrsim$100 Mpc) and current EM sensitivity limits.

More broadly, fast ejecta contributes to the nonthermal afterglow generated by outgoing mass interacting with the interstellar medium (Nakar & Piran 2011). In particular, fast ejecta has been proposed as a possible origin for the X-ray excess detected from GW 170817 3 yr after the merger (Hajela et al. 2021; Nedora et al. 2021). Small quantities ($\sim 10^{-8}$–$10^{-7}\,M_{\odot}$) of fast ejecta have also been proposed to account for the overall properties of the prompt gamma-ray burst emission from GW 170817 via breakout of a jet

from a rapidly expanding cloud (Beloborodov et al. 2020). Finally, fast ejecta can also be produced in eccentric mergers, which can produce nearly head-on collisions at much higher radial velocities than in quasi-circular mergers (e.g., Gold et al. 2012; Chaurasia et al. 2018; Papenfort et al. 2018).

The reliability of ejecta masses from grid-based simulations is tied to how well the collision is spatially resolved, however. The spatial resolution of these simulations is usually limited by computational resources, with the finest grid spacings used to date being 63–86 m (Kiuchi et al. 2017). Properly resolving the surface layers of the star requires grid sizes <10 m (Kyutoku et al. 2014).

Here, we perform a numerical experiment to assess the spatial resolution dependence of fast ejecta from the collision interface of BNS mergers in grid-based hydrodynamic simulations. To decrease the computational cost, we solve the Newtonian hydrodynamics equations in two-dimensional (2D) cylindrical symmetry with self-gravity in a corotating frame, to account for orbital motion, and with an approximate prescription for orbital decay due to GWs. These approximations, while losing accuracy relative to a full three-dimensional (3D) setting, preserve the qualitative feature of two sharp stellar edges colliding under the relevant force environment, and allow us to reach grid sizes as low as 4 m ($\sim 3 \times 10^{-4}$ of the NS radius).

The structure of the paper is the following. Section 2 describes our physical assumptions, computational method, and choice of models. Our results are presented in Section 3, with a general overview of our baseline model, parameter dependencies, and comparison with previous work. The observational implications of our results are presented in Section 4, and a summary and discussion follows in Section 5.

2. Methods

2.1. Physical Model and Approximations

Our goal is to study the ejection of material during the initial collision between the merging NSs and its immediate aftermath, with a focus on the high-velocity tail of the ejecta velocity distribution. Our numerical experiment attempts to capture the key features of the stellar collision in 2D, which allows for a much higher spatial resolution than is achievable in a full 3D configuration.

The hydrodynamic interaction between the two stars is influenced primarily by three effects: gravity, orbital motion, and orbital decay due to GW emission. Correspondingly, we neglect neutrino processes, magnetic fields, and stellar rotation in our study. While these effects can certainly influence mass ejection, they either provide subdominant corrections to the main processes considered here, or in the case of magnetic fields, introduce complications for comparing with previous work. Additionally, we do not keep track of the ejecta composition, and assess the feasibility of r-process freeze out based on ejecta velocity, which is a good proxy for expansion time (Metzger et al. 2015).

We model the NS binary geometry in 2D by adopting an axisymmetric cylindrical coordinate system, positioning the stars along the symmetry ($\hat{z}$) axis, thereby accounting for their spherical geometry along the azimuthal ($\hat{\varphi}$) direction. We then set the orbital angular momentum vector aligned with the cylindrical radial ($\hat{r}_{\rm cyl}$) axis, with orbital motion occurring along a pseudo-azimuthal vector $\hat{\xi} = -\mathrm{sgn}(z)\hat{\varphi}$ around this axis (Figure 1).

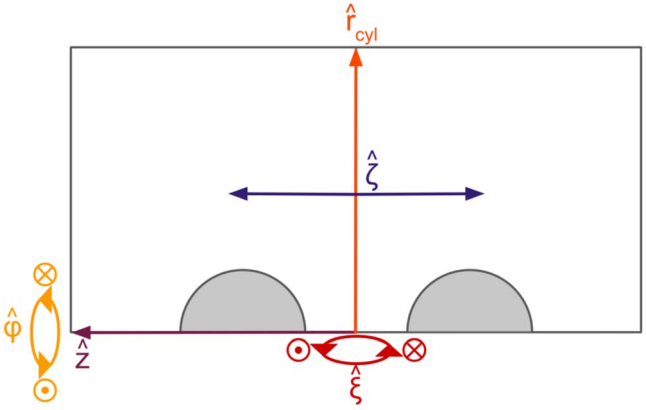

Figure 1. Schematic of the coordinate system used. An axisymmetric domain in cylindrical coordinates ($r_{\rm cyl}$, φ, z) is rotated 90° counterclockwise and the stars are placed along the symmetry axis (z). The orbital angular momentum vector points in the cylindrical radial ($r_{\rm cyl}$) direction. Orbital motion occurs along the pseudo-azimuthal vector $\hat{\xi} = -\mathrm{sgn}(z)\hat{\varphi}$ and the distance from the rotation axis is described by the auxiliary vector $\hat{\zeta} = \mathrm{sgn}(z)\hat{z}$.

Orbital motion is quantified with a specific angular momentum scalar $j = \omega z^2$, where $\omega(r_{\rm cyl}, z, t)$ is the orbital angular velocity (t is time). We work in a corotating coordinate system around $\hat{r}_{\rm cyl}$ with constant angular frequency $\omega_0 = 2\pi/t_{\rm dyn}$, where

$$t_{\rm dyn} = \left[\frac{4\pi^2}{G(M_1 + M_2)} d_0^3\right]^{1/2} \quad (1)$$

is the initial (Newtonian) orbital period of the system, with d_0 the initial separation between the stellar centers, and $M_{1,2}$ the stellar masses.

The centrifugal acceleration in this corotating frame is then

$$\boldsymbol{f}_{\rm cen} = \omega_0^2 |z|\,\hat{\zeta} = \omega_0^2 |z|\,\mathrm{sgn}(z)\hat{z} = z\omega_0^2\,\hat{z}, \quad (2)$$

where $\hat{\zeta} = \mathrm{sgn}(z)\hat{z}$ is a unit vector that points away from the orbital axis (Figure 1). The Coriolis acceleration is given by

$$\boldsymbol{f}_{\rm cor} = 2\omega_0[v_\xi\hat{\zeta} - v_\zeta\hat{\xi}] = 2\omega_0\,\mathrm{sgn}(z)[v_\xi\hat{z} - v_z\hat{\xi}], \quad (3)$$

where

$$v_\xi = \frac{j}{|z|} - |z|\omega_0 \quad (4)$$

is the corotating frame velocity along $\hat{\xi}$, $v_\zeta = \mathrm{sgn}(z)v_z$ is the speed away from the orbital angular momentum axis, and v_z is the velocity along $\hat{z}$. With this formulation, matter moving toward the axis ($v_\zeta < 0$) is accelerated in the $+\hat{\xi}$ direction, while matter rotating faster than the coordinate system ($v_\xi > 0$) is pushed away from the rotation axis ($+\hat{\zeta}$), thus following the standard behavior of the Coriolis force. The azimuthal term in the Coriolis acceleration acts as a source term for the specific angular momentum

$$\left(\frac{\partial j}{\partial t}\right)_{\rm cor} = (\boldsymbol{r} \times \boldsymbol{f}_{\rm cor})_{r_{\rm cyl}} = -2\omega_0 z v_z. \quad (5)$$

We neglect other components of the torque given the symmetry of our coordinate system (the ζ component of the Coriolis acceleration adds or subtracts from the centrifugal acceleration).

The correctness of this formulation is verified by the maintenance of a stable Keplerian orbit in the absence of GW losses (Section 2.2). A schematic of the relative direction of the inertial accelerations is shown in Figure 2.

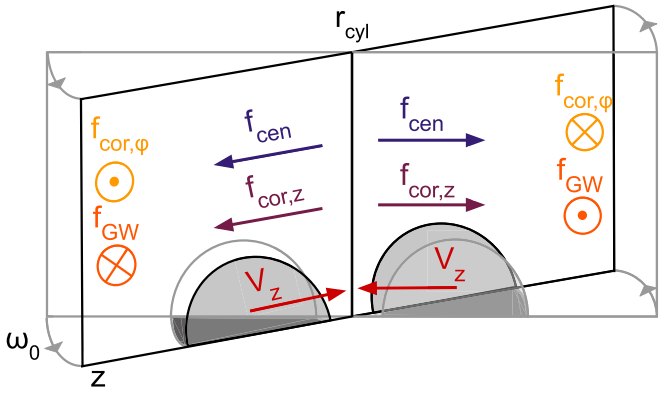

Figure 2. Schematic of the numerical experiment. A corotating frame is employed, with constant angular velocity ω_0 set to the initial Keplerian value. Matter thus experiences centrifugal and Coriolis accelerations (Equations (2) and (3)). Orbital motion is quantified with a space- and time-dependent specific angular momentum scalar $j = \omega z^2$, which can be modified by the component of the Coriolis acceleration in the orbital direction (Equation (5)) and by GW emission (Equation (15)). The stars with masses M_1 and M_2 are initialized at an initial separation d_0 measured from their centers, with the center of mass at the origin, and with velocities in the z-direction toward the rotation axis, resulting in the acceleration directions shown. The intrinsic symmetry of the cylindrical coordinate system accounts for the sphericity of the stars.

2.2. Numerical Hydrodynamics

We use `FLASH` version 4.5 (Fryxell et al. 2000; Dubey et al. 2009) to solve the equations of Newtonian hydrodynamics in 2D cylindrical coordinates in a corotating frame, with source terms due to self-gravity and GW losses:

$$\frac{\partial \rho}{\partial t} + \nabla \cdot (\rho \boldsymbol{v}) = 0, \tag{6}$$

$$\frac{D\boldsymbol{v}}{Dt} = -\frac{\nabla P}{\rho} - \nabla\Phi + \boldsymbol{f}_{\rm cen} + (\boldsymbol{f}_{\rm cor} \cdot \hat{\zeta})\hat{\zeta}, \tag{7}$$

$$\frac{Dj}{Dt} = \left(\frac{\partial j}{\partial t}\right)_{\rm gw} + \left(\frac{\partial j}{\partial t}\right)_{\rm cor}, \tag{8}$$

$$\frac{D\epsilon}{Dt} - \frac{P}{\rho^2}\frac{D\rho}{Dt} = 0, \tag{9}$$

$$\nabla^2\Phi = 4\pi G\rho, \tag{10}$$

where $D/Dt \equiv (\partial/\partial t + \boldsymbol{v}\cdot\nabla)$, $\boldsymbol{v} = v_{\rm rcyl}\hat{r}_{\rm cyl} + v_z\hat{z}$ is the poloidal velocity, ρ is the density, P is the total gas pressure, ϵ is the total specific internal energy, Φ is the gravitational potential, and G is the gravitational constant. The system of equations is solved with the dimensionally split piecewise-parabolic method (PPM; Colella & Woodward 1984), the multipole self-gravity solver of Couch et al. (2013), and is closed with a piecewise polytropic equation of state (EOS).

The EOS contains a cold component with four segments,

$$P_{{\rm c},i} = K_i \rho^{\Gamma_i} \quad i = \{0, 1, 2, 3\}, \tag{11}$$

where the adiabatic indices Γ_i, transition densities ρ_i, and transition pressure $P_{\rm c,1}$ are taken from Read et al. (2009). This cold component connects continuously at low density to a `SLy` EOS for the crust (Douchin & Haensel 2001). The EOS also includes a thermal component (e.g., Bauswein et al. 2010), such that the total pressure satisfies

$$P = P_{\rm c} + P_{\rm th}, \tag{12}$$

$$P_{\rm th} = (\Gamma_{\rm th} - 1)\rho\epsilon_{\rm th}, \tag{13}$$

$$\epsilon_{\rm th} = \epsilon - \epsilon_{\rm c}., \tag{14}$$

where the subscripts "c" and "th" denote the cold and thermal components, respectively. We adopt $\Gamma_{\rm th} = 5/3 \simeq 1.67$ as an intermediate value in the interval [1.5, 2], which was found by Bauswein et al. (2010) to bracket the behavior of microphysical, finite-temperature EOSs.

We include the effect of GW losses on the orbit through a source term that modifies the specific angular momentum

$$\left(\frac{\partial j}{\partial t}\right)_{\rm gw} = \frac{1}{2}\frac{j}{d}\left(\frac{\partial d}{\partial t}\right)_{\rm gw}, \tag{15}$$

where we assume a Keplerian dependence on the instantaneous orbital separation d between the centers of mass of each star (semimajor axis of the reduced mass), $j \propto d^{1/2}$. The rate of change of d is taken to be the standard expression for two point masses with $e = 0$ (Peters 1964),

$$\left(\frac{\partial d}{\partial t}\right)_{\rm gw} = -\frac{64}{5}\frac{G^3}{c^5}\frac{(M_1 + M_2)M_1M_2}{d^3}. \tag{16}$$

While these equations are strictly valid only for point masses, we apply this source term to all stellar material that has nonzero j (i.e., material ejected after the collision). Once j reaches zero, the source term is also set to zero. For equal-mass binaries, we set $d = 2|z|$ in Equations (15) and (16). For asymmetric binaries, we need to account for the mass ratio $q = M_2/M_1$, and hence set $d = (1 + 1/q)|z_1|$ or $d = (1 + q)|z_2|$ for all matter on the side of star 1 or star 2 relative to $z = 0$, respectively. Aside from this substitution, the mass ratio dependence scales out of Equation (15).

The computational domain spans the range [0, 90] km in $r_{\rm cyl}$ and [−90, 90] km in z, and is discretized with a uniform grid with square cells $\Delta r_{\rm cyl} = \Delta z$. We choose our resolution in relation to the pressure scale height $H_{\rm p} = P/(\rho|\nabla\Phi|)$ near the stellar surface (Figure 3). Given the numerical dissipation properties of the PPM (e.g., Porter & Woodward 1994), we consider a length scale as resolved if we can cover it with 10 computational cells. Our baseline grid spacing is $\Delta r_{\rm cyl} = \Delta z = 32$ m in all models (Section 2.3), which resolves the pressure scale height out to ∼93% of the stellar radius. Our finest resolution, $\Delta r_{\rm cyl} = \Delta z = 4$ m, reaches beyond 99.9% of the stellar radius $R_{\rm ns}$, enclosing all but the outermost $\sim 9 \times 10^{-4}\, M_\odot$ of the stellar mass.

The boundary conditions are reflecting at $r_{\rm cyl} = 0$, and outflow at all other domain limits. The orbital configuration is tested by initializing the stars in a Keplerian orbit, with an initial separation $d_0 \simeq 8R_{\rm ns}$, and verifying that the stars maintain their initial positions in the absence of GW losses, with only minor in-place oscillations. Based on this stationarity test we employ 128 multipoles for self-gravity in all of our runs.

2.3. Initial Conditions

Neutron stars are constructed by solving the Newtonian hydrostatic equilibrium equations using the EOSs described in Section 2.2. We test the solution by evolving an isolated star centered at the origin for 10 stellar dynamical times $\tau_{\rm dyn}^{\rm ns} \simeq (2\pi)^{-1}(R_{\rm NS}/d_0)^{3/2}\, t_{\rm dyn}$, and verify that it remains close to a steady state with low kinetic energy (Figure 4).

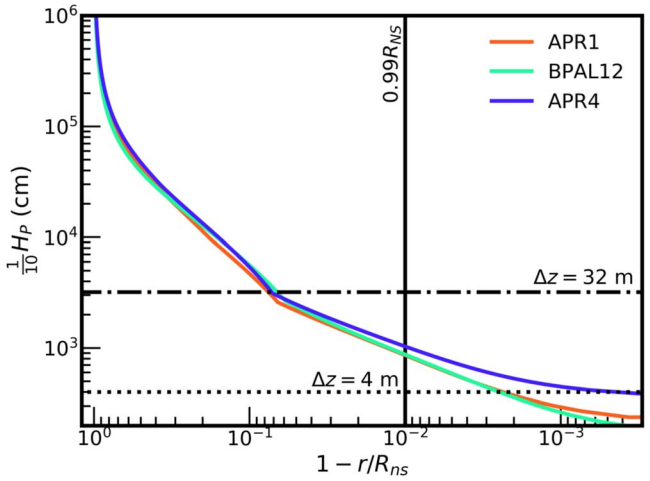

Figure 3. Spatial resolution in terms of relevant length scales in the problem. Solid curves show 1/10 of the pressure scale height H_p as a function of exterior radius in a 1.4 $M_\odot$ NS constructed with the APR4 EOS (purple), BPAL12 EOS (teal), and APR1 EOS (orange). Also shown as horizontal lines are our baseline resolution $\Delta r_{cyl} = \Delta z = 32$ m (dotted–dashed) and the finest resolution used, $\Delta r_{cyl} = \Delta z = 4$ m (dotted). The latter covers H_p with 10 cells out to >99.9% of the stellar radius, corresponding to an exterior mass of $<9 \times 10^{-4}\ M_\odot$ for the APR4 EOS.

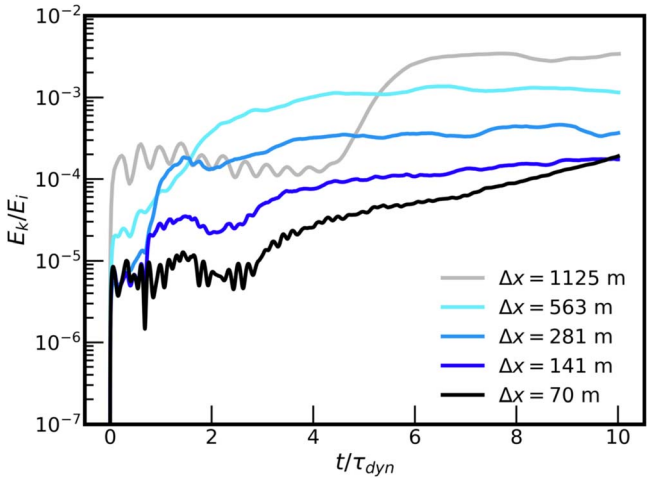

Figure 4. Hydrostatic equilibrium test of an isolated $1.4M_\odot$ NS constructed with the APR4 EOS at the center of the computational domain, showing the ratio of kinetic energy E_k to internal energy E_i in stellar material as a function of time, in units of the dynamical time of the star $\tau_{dyn} \simeq 0.07$ ms. Curves correspond to different spatial resolutions, as labeled.

Simulations are initialized with the two stellar centers placed on the z-axis at a separation d_0 slightly larger than the sum of the stellar radii, and located such that the center of mass of the system is at the origin, $|z_1/z_2| = M_2/M_1 = q$, with $|z_1|$ and $|z_2|$ the initial z coordinates of the corresponding stellar centers

In our default configuration, the interior of each star is assigned the Keplerian velocity of the center of mass uniformly, with a correction for the inspiral of the orbit,[4] thus initially $v_\xi \simeq 0$ at the center of mass of each star. The initial velocity along the z-axis is set to the value implied by the decay rate of the orbital separation due to GW emission (Equation (16)), with a characteristic magnitude $\sim 2 \times 10^9$ cm s^{-1}. To probe the sensitivity of our results to the initial conditions, we also evolve a head-on collision model that removes rotation, inertial forces, and GW losses, as well as one that sets the velocity along the z-axis to the freefall value.

The stars are initially embedded in an ambient medium of mass $\sim 2.3 \times 10^{-8}\ M_\odot$, density 10^4 g cm^{-3}, and constant pressure 10^{25} dyn cm^{-2}, with the remaining thermodynamic variables determined by the EOS. The ambient mass is negligible relative to characteristic ejecta masses of interest, and hence it should not significantly influence the velocity of this ejecta.

2.4. Models Evolved

Table 1 shows all of our models and their initial parameters. Our baseline case consists of two NSs with equal mass $M_1 = M_2 = 1.4\ M_\odot$ built with the APR4 EOS (Akmal et al. 1998), yielding a radius $R_{ns} = 12.6$ km. This lies within the radius range allowed by GW 170817 (Abbott et al. 2018), thus yielding a realistic compactness. The default spatial resolution is $\Delta r_{cyl} = \Delta z = 32$ m, and the default evolution time is $\simeq 1.2\ t_{dyn}$ (Equation (1)), corresponding to 1.6 ms. This time interval is sufficient to achieve complete ejection of fast material in our simulations.

To probe the effect of spatial resolution, the fiducial configuration is also evolved at grid spacings $\Delta z = \{281, 141, 70\}$ m, which overlap with values used in previous 3D numerical relativity simulations of BNS mergers. The lower computational cost of these models allow us to evolve them for $\simeq 12\ t_{dyn}$, or 16 ms. Two high-resolution models that employ $\Delta z = \{16, 4\}$ m are evolved for $\simeq 1.2\ t_{dyn}$ to test for convergence.

We probe the effect of varying the EOSs—and thus the compactness of the NSs—with two models that use APR1 (Akmal et al. 1998) and BPAL12 (Zuo et al. 1999), which yield NS radii 11 and 14.1 km for a stellar mass 1.4 $M_\odot$, respectively. All other simulation parameters (aside from the initial separation, which depends on the stellar radius) are identical to those in the default configuration.

Likewise, we probe the effect of our force prescription by evolving two models that remove rotation, inertial forces, and GW losses from the baseline configuration. In one case (model OR, *on rails*), we leave the initial collision velocity along z unchanged from the baseline configuration, corresponding to the rate of decay of the orbital separation by GWs (Section 2.2). The other model (FF) sets the collision velocity to the freefall speed. Both of these models are evolved at the default resolution as well as at coarser grid sizes $\Delta z = 141$, 70 m, to probe the sensitivity to mass ejection to this parameter (models OR70, OR141, FF70, and FF141).

The effect of changing the total binary mass at constant mass ratio is studied with models M1.2_1.2 and M1.7_1.7, which set the total mass to $1.2 + 1.2\ M_\odot$ and $1.7 + 1.7\ M_\odot$, respectively. We ignore here the possibility of prompt collapse, which is possible for the model with the highest total mass. Models M1.5_1.3 and M1.6_1.2 keep the total mass constant at 2.8 $M_\odot$, but change the mass ratio to $q = 0.87$ ($1.5\ M_\odot + 1.3\ M_\odot$) and $q = 0.75$ ($1.6\ M_\odot + 1.2\ M_\odot$), respectively. The initial stellar positions and velocities of these asymmetric cases are consistent with the description in Section 2.3.

[4] This correction is obtained by assuming energy conservation in an orbit decaying by GWs, and is negligible for $d \gtrsim 2R_{NS}$. It is nevertheless included for completeness.

Table 1
Models Evolved and Results

Model	EOS	Inertial Force Treatment	M_1 ($M_\odot$)	M_2 ($M_\odot$)	$R_{1.4}$ (km)	Δx (m)	$M_{\rm ej}$ ($M_\odot$)	$M_{v\geqslant 0.6c}$ Total	$M_{v\geqslant 0.6c}$ Contact ($M_\odot$)	$M_{v\geqslant 0.6c}$ Orbital	E_k >0.3c (10^{49} erg)	E_k >0.6c (10^{49} erg)
base	APR4	All forces	1.4	1.4	12.6	32	2.5×10^{-5}	1.4×10^{-5}	1.3×10^{-5}	6.6×10^{-8}	1.0	0.83
R281*						281.3	1.9×10^{-5}	8.0×10^{-6}	8.0×10^{-6}	6.4×10^{-8}	0.57	0.35
R141*						140.6	2.7×10^{-5}	1.5×10^{-5}	1.5×10^{-5}	1.8×10^{-8}	1.0	0.79
R70*						70.3	2.8×10^{-5}	1.5×10^{-5}	1.5×10^{-5}	6.3×10^{-8}	1.2	0.98
R16						16.0	2.2×10^{-5}	1.1×10^{-5}	1.1×10^{-5}	1.0×10^{-7}	0.98	0.78
R4						4.0	2.6×10^{-5}	1.2×10^{-5}	1.2×10^{-5}	1.2×10^{-7}	1.0	0.77
APR1	APR1				11.0	32	5.4×10^{-5}	2.6×10^{-5}	2.6×10^{-5}	5.4×10^{-7}	2.6	2.1
BPAL12	BPAL12				14.1		1.4×10^{-6}	1.3×10^{-8}	1.3×10^{-8}	1.1×10^{-10}	0.02	0.0006
OR	APR4	On rails			12.6		1.3×10^{-2}	5.7×10^{-3}	2.2×10^{-3}	3.6×10^{-3}	430	300
OR70						70.3	1.6×10^{-2}	6.4×10^{-3}	1.9×10^{-3}	4.5×10^{-3}	520	360
OR141						140.6	1.3×10^{-2}	7.0×10^{-3}	1.7×10^{-3}	5.3×10^{-3}	460	360
FF		Freefall				32	3.6×10^{-2}	1.2×10^{-2}	1.5×10^{-4}	1.2×10^{-2}	950	530
FF70						70.3	3.2×10^{-2}	9.1×10^{-3}	2.0×10^{-4}	8.9×10^{-3}	830	410
FF141						140.6	3.9×10^{-2}	1.1×10^{-2}	2.0×10^{-4}	1.1×10^{-2}	940	510
M1.2_1.2		All forces	1.2	1.2		32.0	1.9×10^{-5}	8.2×10^{-6}	8.2×10^{-6}	2.5×10^{-8}	0.74	0.53
M1.7_1.7			1.7	1.7			5.0×10^{-5}	2.5×10^{-5}	2.5×10^{-5}	8.0×10^{-7}	1.9	1.5
M1.5_1.3			1.5	1.3			2.7×10^{-4}	2.7×10^{-5}	2.7×10^{-5}	5.1×10^{-7}	5.1	1.2
M1.6_1.2			1.6	1.2			2.5×10^{-4}	1.4×10^{-5}	1.2×10^{-5}	1.6×10^{-6}	4.5	0.61

Note: Columns from left to right show model name, EOS, inertial force setup as defined in Section 2.3, NS masses, radius of a 1.4 $M_\odot$ NS, cell size ($\Delta z = \Delta r_{\rm cyl}$), total unbound mass ejected, fast ($v_r \geqslant 0.6c$) unbound ejecta, cumulative kinetic energy of matter traveling at $v_r > 0.3c$ and similarly for $v > 0.6c$. The latter is shown in the last three columns as total amount, and broken up by angular direction. Ejecta masses represent cumulative amounts launched by the end of the default simulation time (1.6 ms). Models marked with a star (low resolution) were evolved 10 times longer than the rest of the set.

3. Results

3.1. Overview of Baseline Model and Resolution Dependence

As the stars collide, mass is ejected on a timescale of ∼1 ms, first in the general direction of the rotation axis, and then toward equatorial regions, as shown in the left row of Figure 5. For analysis, we divide the ejection directions into *contact* plane and *equatorial* plane by a surface 30° from the z-axis (the contact plane being the region that includes the rotation axis). Ejected material is considered unbound from the system when it has positive Bernoulli parameter:

$$\mathrm{Be} = \frac{1}{2}\boldsymbol{v}^2 + \epsilon + \frac{P}{\rho} + \Phi > 0. \quad (17)$$

We sample the unbound mass flux at a spherical extraction radius $r_{\rm out} = 30$ km from the origin[5] (the z-axis is the symmetry axis for the mass ejection measurement sphere). *Fast* ejecta is defined as that with radial velocity $v > 0.6c$ at $r = r_{\rm out}$, while *slow* ejecta is that with $v < 0.6c$.

Mass ejection is episodic (Figure 6), with two initial bursts of mostly fast ejecta, up to a time of $\sim 0.4\, t_{\rm dyn} \simeq 0.5$ ms. Thereafter, slow ejecta continues to build up beyond $\sim 1\, t_{\rm dyn} \simeq 1.4$ ms. Each of these episodes is the result of oscillations in the collision remnant, as seen in global 3D merger simulations (e.g., Bauswein et al. 2013). These oscillations show as steps in the cumulative ejected mass as a function of time in Figure 6. While contact plane ejecta appears in only two bursts, with marginal increases thereafter, orbital plane ejecta gradually builds up through several oscillations, with the average velocity of the ejected material decreasing with time. The vast majority of the fast ejecta is launched toward the contact plane direction in this model.

Note that on the timescale of our simulation, production of fast ejecta is largely complete, while the slow ejecta is still increasing (Figure 6). We thus find total ejecta masses (fast and slow) that are significantly lower than those typically reported in global 3D merger simulations for this binary combination ($\gtrsim 10^{-3}\, M_\odot$, e.g., Hotokezaka et al. 2013; Rosswog 2013; Lehner et al. 2016; Sekiguchi et al. 2016; Bovard et al. 2017; Dietrich et al. 2017; Radice et al. 2018).

Figure 6 also shows that the mass ejection history is qualitatively the same in the baseline model and in the highest resolution model (R4). In particular, the contact plane ejecta is the same within 10%. While larger changes with resolution up to a factor ∼2 are seen in the fast material ejected toward equatorial latitudes, this contribution is subdominant compared to matter ejected toward the contact plane.

The effect of spatial resolution on the angle and velocity distribution of cumulative unbound ejecta is shown in Figure 7. This sequence of models spans a factor of ≃70 in resolution, from the coarsest grid size $\Delta r_{\rm cyl} \simeq 280$ m to the finest value at 4 m. While the overall shape of these two-dimensional histograms is the same in all cases, the most visible change occurs for matter within ∼30° of the rotation axis, i.e., contact plane ejecta. As the resolution is increased, more mass is ejected around the rotation axis at the high and low velocity ends. Note that since our simulations are Newtonian, a small amount of mass achieves $v > c$.

Taking the fast ejecta from model R4 as a baseline, we estimate the degree of convergence of mass ejection by computing differences relative to this ejecta value as a function of resolution. Figure 8 shows that the total fast ejecta mass converges as $\Delta r_{\rm cyl}^{0.46}$ over the entire resolution range explored. Convergence to within 10% is achieved for $\Delta r_{\rm cyl} \approx 19.7$ m.

[5] Changing the position of this extraction radius can change the inferred fast ejecta mass by a factor ∼2.

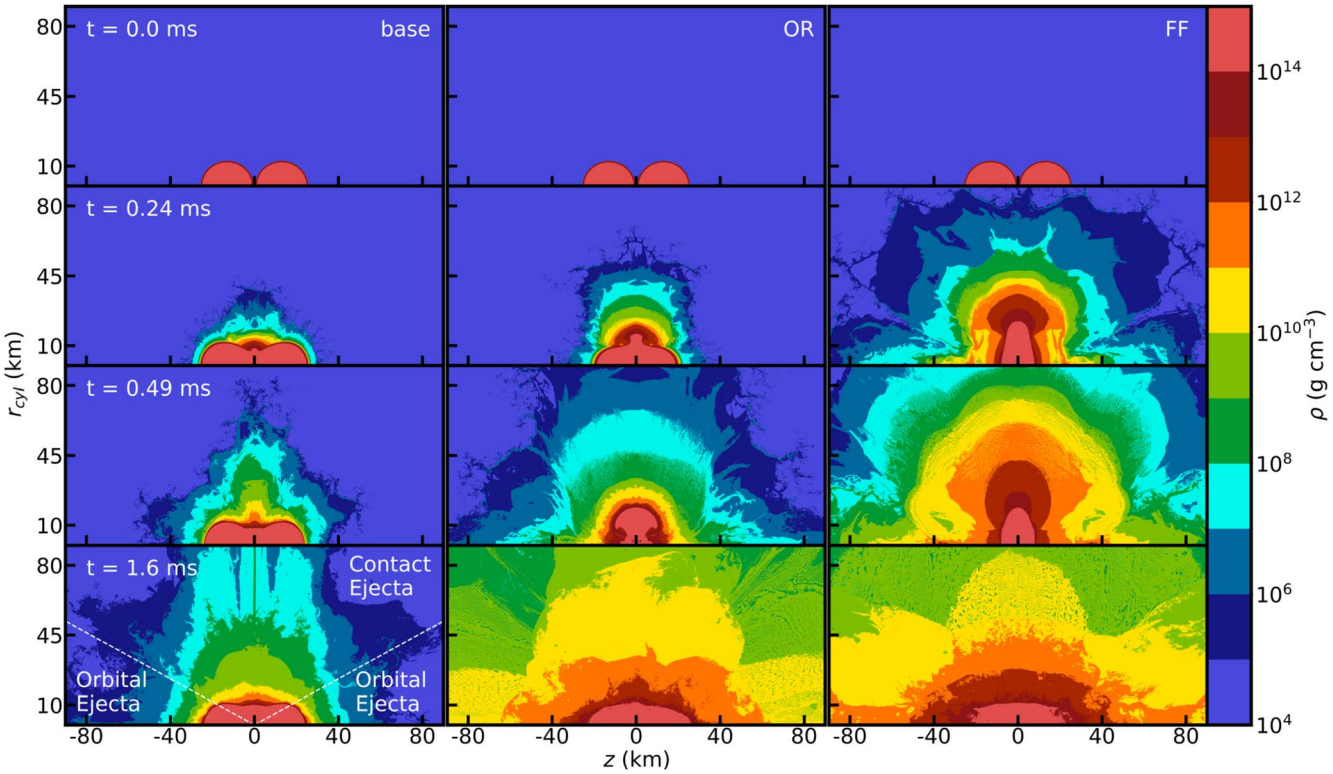

Figure 5. Left: snapshots in the evolution of the `base` model (see Table 1), showing mass density at various times, as labeled. The white dotted line at 30° from the z-axis shows the division between *contact* plane and *orbital* plane directions, as labeled. Middle: same as in the left column but removing orbital motion, inertial forces, and gravitational wave losses (model `OR`). Right: a head-on collision at the freefall speed (model `FF`), for comparison.

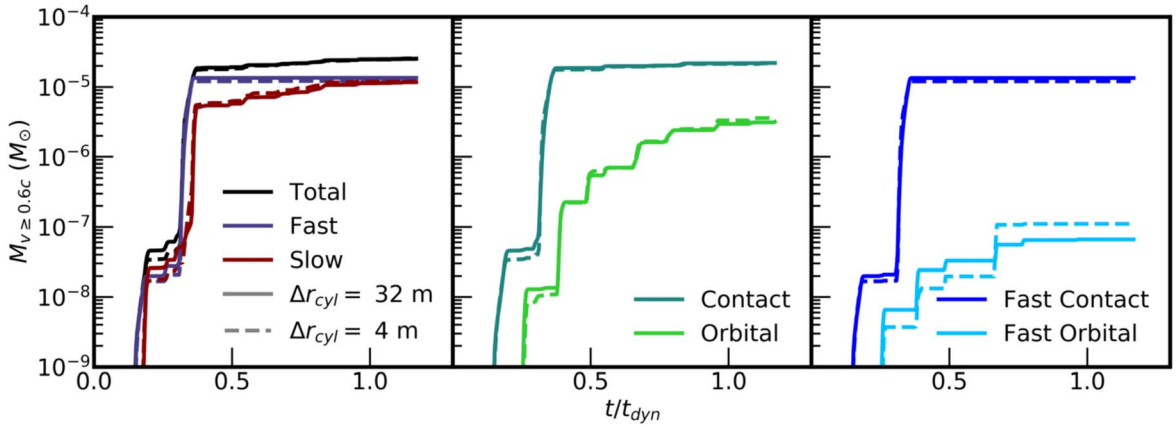

Figure 6. Time dependence of mass ejection in model `base` (solid lines) and `R4` (dashed lines, highest resolution), as measured from a spherical sampling surface with a radius 30 km from the origin. Left: unbound ejecta separated into fast ($v > 0.6c$) and slow ($v < 0.6c$). Middle: total unbound ejecta separated into angular directions (see Figure 5). Right: fast ejecta separated into angular directions.

A natural explanation of this trend with cell size is the increasing degree by which the stellar edges are resolved (Figure 3). Overall, fast ejecta on the contact plane can change by a factor of ∼2 from the lowest to highest resolution (Table 1). The equatorial ejecta also increases by a factor of ∼2 over the entire resolution range. Spatial resolution therefore also has an effect on matter ejected during remnant oscillations (as inferred from Figure 6) even though the overall shape of the equatorial ejecta distribution remains largely the same in Figure 7. Again, equatorial ejecta contributes primarily with $v < 0.6c$ in this model.

The total fast ejecta from our default configuration across the resolution range we explore is shown in Figure 9, where the very mild dependence with resolution is apparent. For comparison, we also show fast ejecta results from the grid-based, global 3D merger simulations of Radice et al. (2018), corresponding to equal-mass 1.35 $M_\odot$ binaries evolved with different resolutions and neutrino prescriptions. Our results suggest that the fast ejecta values from Radice et al. (2018) are already close to convergence, and are unlikely to increase (for higher resolution) by the magnitude required to match the amount inferred by Metzger et al. (2015) from the SPH simulations of Bauswein et al. (2013).

We also note that the initial burst in the `base` model ejects $\sim 10^{-8}$–$10^{-7}\,M_\odot$ (Figure 6), which has similar magnitude to the ultrarelativistic envelope envisioned by Beloborodov et al. (2020) as a breakout medium for the jet in order to account for

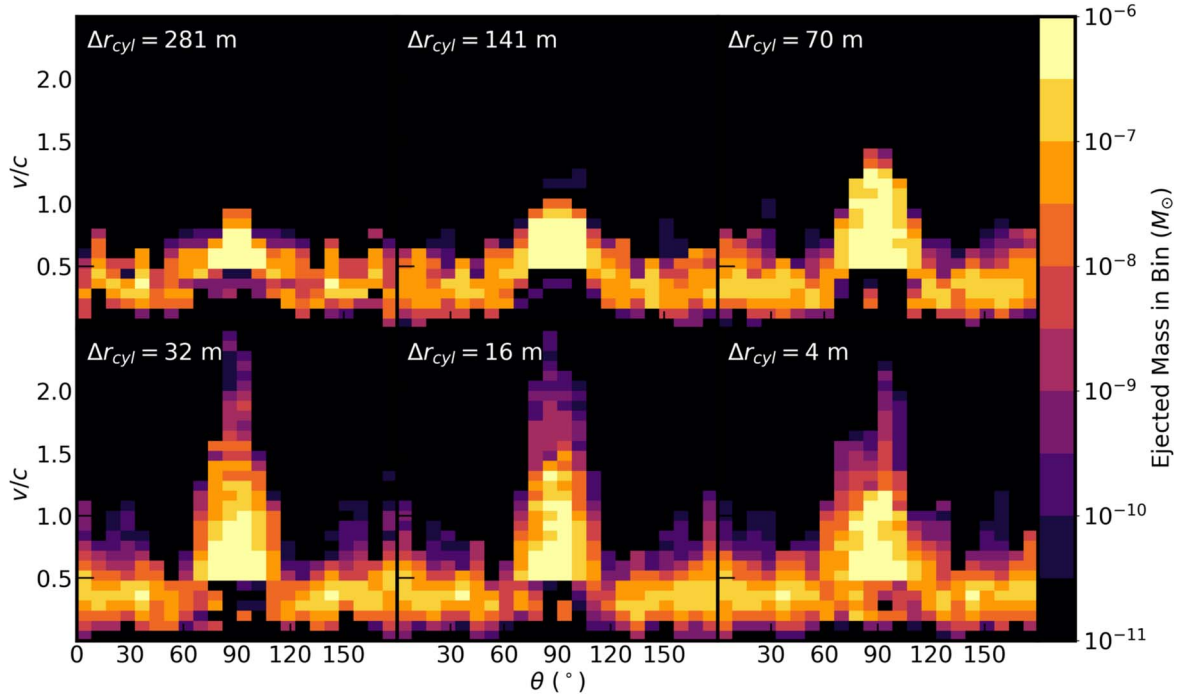

Figure 7. Mass histogram of unbound ejecta as a function of ejection polar angle (measured from the z-axis, see Figure 5, 90° corresponds to the rotation axis) and velocity, for our default binary configuration. Different panels correspond to different spatial resolutions, as labeled (see Table 1, the panel for $\Delta r_{\rm cyl} = 32$ m corresponds to the `base` model). Since our simulations are Newtonian, a small amount of mass can achieve speeds larger than the speed of light.

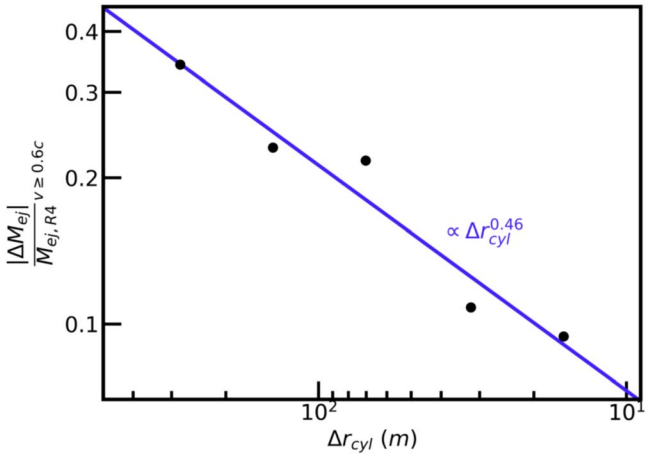

Figure 8. Convergence of fast ejecta mass with spatial resolution. Shown are relative differences in total fast ejecta mass relative to that from model R4. The purple line is a power-law fit.

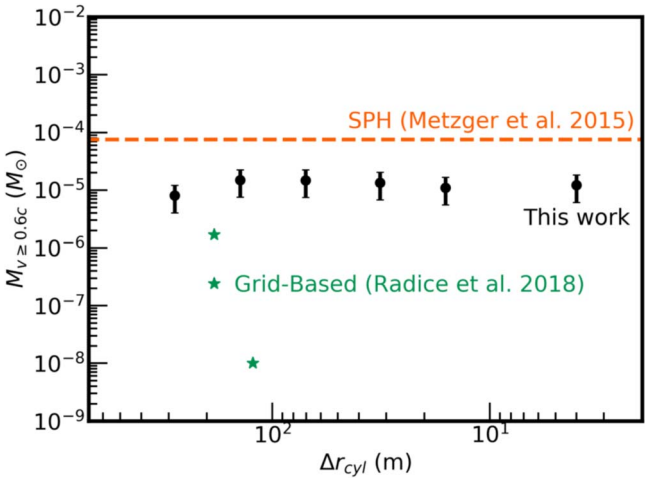

Figure 9. Total fast ejecta for our default configuration (black circles) as a function of cell size (see Table 1). The orange dashed line shows the r-process freeze-out ejecta reported in Metzger et al. (2015) out of the equal-mass 1.35 $M_\odot$ merger simulation from Bauswein et al. (2013), carried out with an SPH code without neutrinos and the `DD2` EOS. Green stars show the fast ejecta reported in Radice et al. (2018) for a set of models with the closest parameters to our `base` case: an equal-mass 1.35 $M_\odot$ binary simulated with a grid code and the `DD2` EOS. The resolutions and neutrino treatment are, from top to bottom, 185 m with an M0 scheme, 185 m with a leakage scheme, and 123 m with a leakage scheme, respectively. We estimate that our values have a measurement uncertainty of a factor ∼2 due to sensitivity to the extraction radius and the imposition of a velocity cut at 0.6c to estimate free neutron masses (Section 3.4).

the features of the prompt emission in GRB 170817A. We caution that for these small amounts of mass, other processes such as neutrino emission and absorption (as envisioned by Beloborodov et al. 2020 to power the expanding envelope) or magnetic fields can be dynamically important and are missing in our simulations. Also, the mass in ambient medium in our models is $\sim 10^{-8}\,M_\odot$ (Section 2.3); hence, the first burst of ejecta is slowed down significantly and its final velocity in our simulations is not physical. Nevertheless, our results suggest the possibility that such a fast moving envelope of small mass could arise from the hydrodynamic interaction alone. Properly capturing this phenomenon will require highly resolved global simulations with neutrino transport and magnetic fields.

3.2. Dependence on Force Prescription and Collision Velocity

As an attempt to quantify the uncertainty in the approximations used in our numerical experiment, we evolve a model (`OR`) in which we remove the corotation of the coordinate system: no orbital motion, and therefore no centrifugal and Coriolis forces

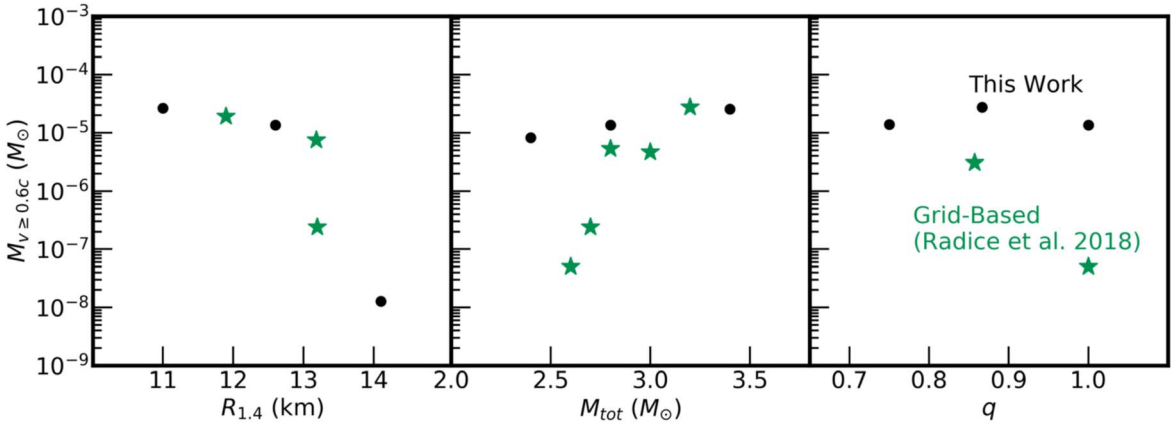

Figure 10. Total fast ejecta from our simulations (black circles), for varying EOS (left), total binary mass (center), and mass ratio (right). See Table 1 for model parameters. For comparison, green stars show a subset of the fast ejecta results from Radice et al. (2018) with the closest parameters. Note that Radice et al. (2018) also reports a merger with compactness that falls between the leftmost two data points in the left panel, which produces no fast ejecta (`LS220_M135135_LK`). Similarly, two runs by Radice et al. (2018) with total masses of 2.4 and 2.5 $M_\odot$ (`DD2_M120120_LK` and `DD2_M125125_LK`) also produce no fast ejecta.

(Section 2.1), as well as no GW losses (Section 2.2). The setting is thus a head-on collision at a speed set by the decay of the semimajor axis due to GWs (Equation (16)).

Figure 5 compares the evolution of model `OR` with our `base` case. Mass ejection occurs at a faster pace, and spans a broader range of latitudes. Ejecta is produced in an episodic manner, with two main bursts occurring during the simulated time, like in model `base`. The second burst is more temporally spread than the first burst in the `base` case, however. Also, while in the latter model both bursts of fast ejecta are predominantly launched toward the contact plane, in model `OR` the first burst is launched toward the contact plane and the second toward the orbital plane. We also note that model `OR` produces more slow ejecta than fast ejecta.

Table 1 shows that the total fast ejecta is a factor ∼300 larger in model `OR` than in the `base` case, with a comparable separation between contact and equatorial plane directions. While the total ejecta mass shows a non-monotonic dependence on spatial resolution, the fast component does vary monotonically, with contact plane ejecta increasing and orbital plane ejecta decreasing with finer grid spacing, and such that the total fast ejecta decreases by ∼20% when going from $\Delta z = 141$–32 m. Lacking the suppressing effect of centrifugal forces, we can take model `OR` as an absolute upper limit to the fast ejecta generated from a binary NS collision.

For reference, we also consider a head-on collision at the freefall speed (model `FF`). Such a calculation has a long history, and the qualitative result is well known (e.g., Shapiro 1980; Rasio & Shapiro 1992; Centrella & McMillan 1993; Ruffert & Janka 1998; Kellerman et al. 2010). This type of collision is astrophysically relevant in the context of eccentric mergers, in which head-on or off-center encounters are a common outcome (e.g., Gold et al. 2012; Chaurasia et al. 2018; Papenfort et al. 2018)

Figure 5 shows that model `FF` behaves in a qualitatively similar way to model `OR`, but due to the higher collision speed, mass ejection occurs at a faster rate. Material first decelerates in the collisional direction as the density gradients meet. The strong pressure gradients produced accelerate material in the contact plane, expanding in that direction before collapsing back and then expanding in the orbital plane direction (e.g., Centrella & McMillan 1993). Over longer time periods, the remnant oscillates in a pattern that alternates between the contact and orbital planes, before settling into a spherical remnant. Model `FF` exhibits two such oscillations of the collision remnant during the 1.6 ms evolution time, resulting in a series of periodic fast ejecta bursts first toward the contact plane, then toward the orbital plane, with the production of fast ejecta saturating before the end of the simulation. We do not follow the oscillation of the remnant for long enough to fully capture all slow ejecta produced, however, which is typically launched by four to six violent oscillations of the remnant, before settling into a spherical shape over a period of ∼3 ms (Ruffert & Janka 1998).

Table 1 shows that mass ejection from model `FF` is significant, with a total fast ejecta reaching 0.01 $M_\odot$. Like in model `OR`, the total unbound ejecta shows a non-monotonic dependence on resolution. While the fast ejecta produced toward the contact plane decreases by ∼25% for increasing resolution, fast ejecta launched toward the orbital plane is dominant by a factor ∼50 and shows non-monotonic behavior.

3.3. Dependence on EOS, Total Mass, and Mass Ratio

When varying the EOS and therefore the NS radius relative to the baseline configuration, we find a monotonically increasing dependence of the quantity of fast ejecta produced on compactness (Figure 10). Our model with the largest NS radius (`BPAL12`) produces ∼1000 times less fast ejecta than our `base` case, even though the total amount of ejecta is lower by a factor of 20 only: the vast majority of dynamical ejecta is slow. The oscillations of the remnant in this case are also much weaker and occur more frequent than in the `base` case, with the production of slow ejecta occurring over four or more bursts during the simulated time in contrast to the two bounces in the `base` case. At the other end, our most compact configuration `APR1` ejects only a factor ∼2 more mass than the `base` model, both fast and slow. More compact stars dive deeper into the gravitational potential upon collision, and therefore more energy becomes available to eject mass. This dependence of dynamical ejecta quantity on compactness is a well-known result from global 3D merger simulations (e.g., Hotokezaka et al. 2013).

The angle-velocity mass histogram (Figure 11) shows that for the least compact model `BPAL12`, the high-velocity tail of the contact plane ejecta disappears, yielding a more uniform distribution in polar angle. The highest compactness model `APR1` shows an extension of the contact plane ejecta to even

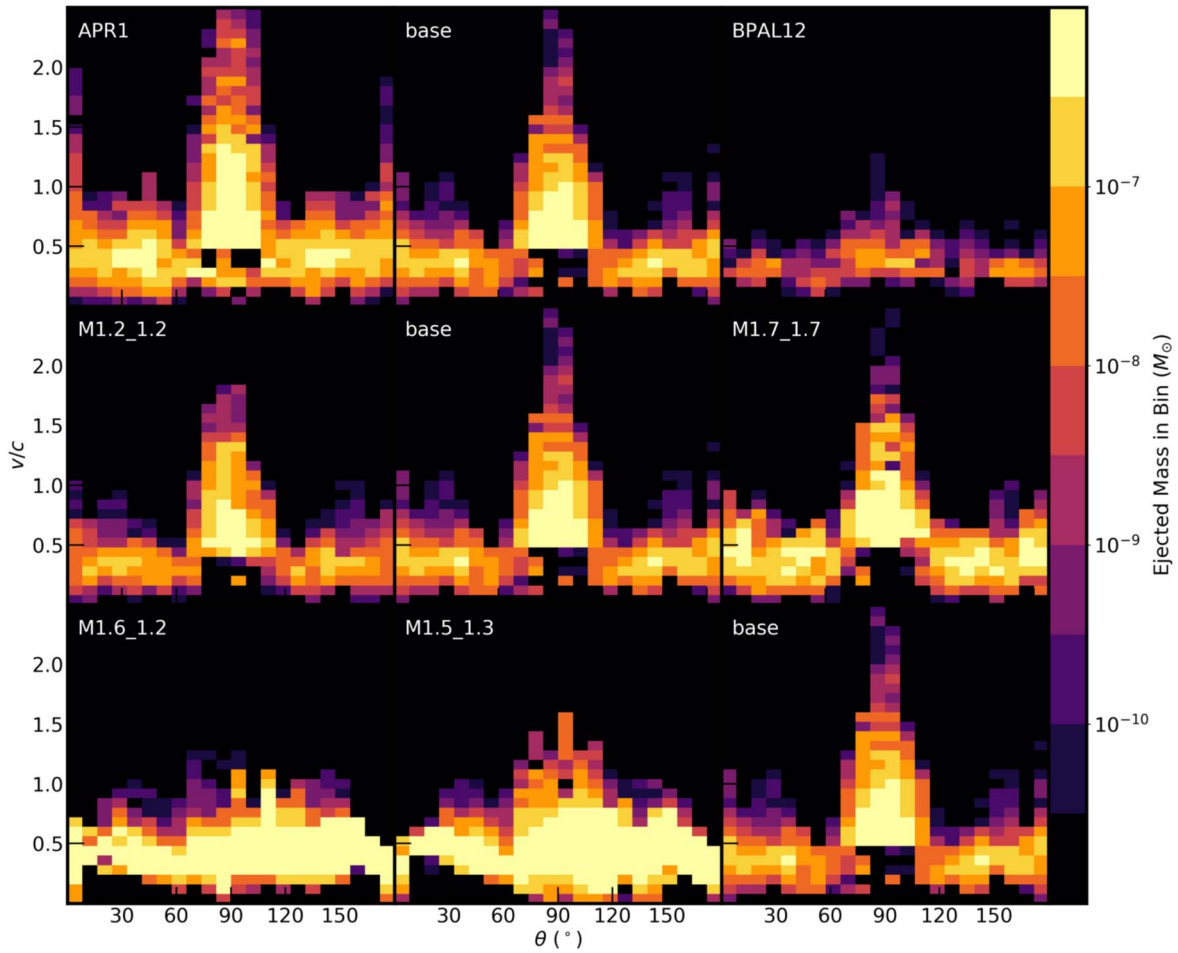

Figure 11. Same as Figure 7 but for models that vary the EOS (top row), total binary mass (middle row), and mass ratio (bottom row), as labeled (see Table 1).

higher velocities, and an increase in the amount of fast equatorial ejecta.

When varying the total mass of the binary system, we find a mild monotonic dependence of fast ejecta with binary mass. Going from a $1.2 + 1.2\,M_\odot$ binary to $1.7 + 1.7\,M_\odot$, we find an increase by a factor $\sim$3 of both fast and slow ejecta masses (Figure 10). Our models, being Newtonian, exclude the possibility of prompt black hole (BH) formation, which is a likely outcome of the model with the highest total binary mass. Prompt BH formation is usually detrimental for mass ejection (e.g., Bauswein et al. 2013; Hotokezaka et al. 2013).

Table 1 shows that in all cases that vary the total mass, the fast orbital plane ejecta remains subdominant compared to that launched toward the contact plane. This is consistent with the angle-velocity mass histogram (Figure 11), which shows very similar results for all three cases that change the total binary mass. For fixed EOS, more massive NSs have smaller radii and therefore larger compactness, again yielding the known trend of higher mass ejection for collisions that reach deeper into the gravitational potential.

Changing the mass ratio at fixed constant binary mass yields a non-monotonic trend in fast ejecta production, with changes in total fast ejecta of a factor $\sim$2 (Figure 10). By increasing the asymmetry of the binary, the number of ejection bursts increases from two bounces in the equal-mass `base` case to four or more oscillations for the asymmetric models (`M1.5_1.3` and `M1.6_1.2`). Additionally, orbital plane ejecta is predominantly launched (factor $\sim$3) in the direction of the smaller star.

Table 1 shows that the majority of fast ejecta continues to be produced toward the contact plane, with overall changes in this subset dominating the overall trend. An additional trend is a sharp increase in the amount of equatorial fast ejecta with decreasing mass ratio by a factor 30 over the range explored. However, even in the most asymmetric case ($1.6 + 1.2\,M_\odot$), the equatorial plane contribution to the fast ejecta is lower by a factor 10 than that from the contact plane. The angle-velocity histogram (Figure 11) shows that increasing the asymmetry of the binary results in a decrease of the high-velocity tail of the contact plane ejecta, and a more isotropic production of ejecta.

3.4. Discussion and Comparison with Previous Work

Our baseline configuration yields fast ejecta quantities that fall in between those found using SPH and grid-based methods, as shown in Figure 9. Given the number of approximations necessary to make our numerical experiment possible, the absolute amount of fast ejecta we find is not the most reliable quantity. Nonetheless, our most important result is that there is little resolution dependence in this fast ejecta when going from typical cell sizes employed in global 3D merger simulations using grid-based codes ($\sim$100 m) to values that can capture the dynamics at the stellar surface reliably (a few meters).

We consider this resolution dependence to be a robust result, for the following reasons. First, the NSs and post-collision remnant are spatially extended on scales $\sim R_{\rm NS}$. The gravitational acceleration should be insensitive to small scale effects,

except if a strong curvature develops. The latter can arise with prompt black BH formation, which is not considered in this study. Of particular concern would be high-mass binaries very close to prompt collapse, in which a change in spatial resolution could drastically change the amount of mass ejected. Second, mass ejected at high speeds becomes length contracted in the laboratory frame. This effect becomes significant for relativistic momenta $\gamma\beta \gtrsim 1$. In both our numerical experiment (Figure 7) and in global 3D merger simulations, the ejecta has a mass distribution that is a decreasing function of velocity. We can estimate the error introduced by ignoring relativistic kinematics by computing the ratio of fast ejecta with $v > c$ to that with $v > 0.6c$ in the `base` model: $M_{v\geqslant c}/M_{v\geqslant 0.6c} \simeq 0.17$. This 20% uncertainty in our fast ejecta values due to the Newtonian description is comparable to the changes with grid spacing in our best-resolved models. For comparison, Radice et al. (2018) finds variations of order a few in fast ejecta mass when increasing the resolution from 185–123 m. Our models yield a similar resolution dependence when changing the grid spacing from 281–141 m.

The choice of extraction radius at 30 km does introduce a degree of uncertainty in the absolute values of fast ejecta that we report. Increasing this extraction radius to 90 km decreases the fast ejecta mass by a factor ∼2 in the base model. Most of this fast ejecta leaves the computational domain before the end of the simulation; therefore, this dependence on the position of the extraction radius implies some degree of slowdown in the vicinity of the collision remnant. Since all simulations are measured with the same extraction radius, however, the position of this surface should not significantly affect changes in fast ejecta with resolution.

Our definition of fast ejecta ($v > 0.6c$) has been adopted to allow direct comparison with previous work. For the purposes of estimating the freeze out of the *r*-process, however, a more strict criterion involves using the expansion time, with the relevant material expanding to densities 4×10^5 g cm^{-3} in less than 5 ms (Metzger et al. 2015). For completeness, we estimate the expansion time of our fast ejecta material. In the absence of tracer particles, we compute this estimate as follows. We first consider the angle-averaged radial profile of the density of ejected material beyond the sampling radius at a time $t = 0.49$ ms (Figure 12), with the average carried out over the contact plane for the `base` model, and over the orbital plane for model `FF`, since these directions contain the majority of the fast ejecta (Table 1). Assuming the material ejection is in steady state, we estimate an upper limit to the expansion time for the `base` model as the crossing time from 30–60 km at $v = 0.6c$, at which point the target density for freeze out is reached. This yields an expansion time of 1.6×10^{-4} s. For the `FF` case, we extrapolate the density profile and find the distance necessary to reach the target density for freeze out, and compute the crossing time at $v = 0.6c$. The result is a slightly longer 5.8×10^{-4} s. In both cases, these simple estimates indicate that our velocity cut at $0.6c$ is more strict than what is needed to achieve neutron freeze out, with a corresponding underestimate of the mass available to power a precursor. Lowering the velocity cut in our numerical experiment would increase our *fast* ejecta at most by a factor of ∼2, however, since our slow ejecta is of comparable magnitude (Table 1). But since global 3D merger simulations produce significantly more slow ejecta, the exact value of the velocity cut can be in part responsible for the large discrepancy with particle-based results. The velocity distribution of ejecta in Figure 1 of Metzger et al. (2015) shows

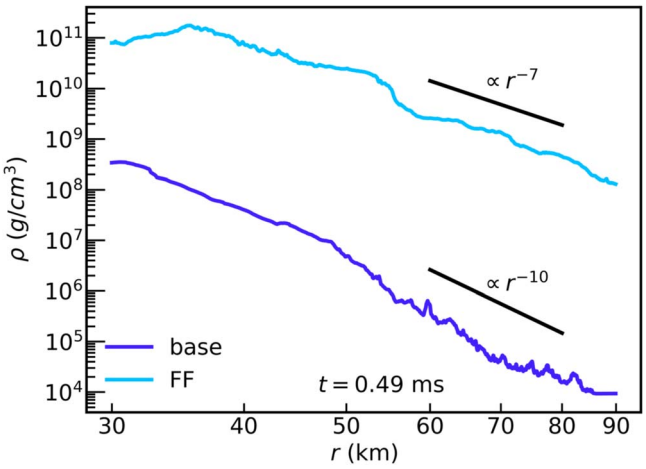

Figure 12. Angle-averaged radial profiles of density at 0.49 ms for models `base` (purple) and `FF` (blue), with the average carried out over the contact and orbital plane directions, respectively. Radial slopes of r^{-7} and r^{-10} are shown for reference.

that there is indeed non-negligible free neutron production for $0.4 < v/c < 0.6$. A more careful analysis of this question requires use of sufficient tracer particles to sample the fraction of the velocity distribution that will yield the ejecta of interest.

Given the extraction radius dependence of our fast ejecta values, and the possibility that more free neutrons can be produced at $v < 0.6c$, we can adopt a fiducial uncertainty of a factor ∼2 in the absolute values of our fast ejecta.

Since most of our simulations are only run long enough for production of fast ejecta to be complete, slow ejecta is still being produced by the end of the simulation. By the end of our `base` model, $2.5 \times 10^{-5}\,M_\odot$ of total ejecta is produced. This is roughly an order of magnitude less ejecta than the closest case in Radice et al. (2018), and about two orders of magnitude less ejecta than was produced in the SPH simulation performed by Bauswein et al. (2013). While short run times (set by computational resources) are partly responsible for this lack of slow ejecta, our lower resolution models (`R281, R141, R70`), which run 10 times longer than the `base` case still do not produce sufficient slow ejecta to match 3D global simulations. For example, model `R70` produces 1% more fast ejecta and a factor of ∼2 more slow ejecta for an increased runtime a factor of 10 longer. The imposition of axisymmetry and other approximations therefore also play a role in this discrepancy.

An important difference between our results and those of Radice et al. (2018) is the way in which most of the fast ejecta is produced, a likely consequence of the approximations made in our study. Radice et al. (2018) finds that fast ejecta emerges in two bursts, first from the contact interface and then from the first bounce of the hypermassive NS (HMNS) remnant. The first burst is not always present, but the HMNS bounce is more robust and dominates the production of fast ejecta. We see a two burst structure in many of our simulations when varying total mass, or EOS (except in the low compactness case `BPAL12`, which produces less contact plane ejecta). This is also apparent in our force prescription variations, with `FF` producing an additional late time burst. This burst structure however is largely a temporal variation, with the majority of the ejecta in each burst being launched in the contact plane, whereas Radice et al. (2018) finds the first burst to be launched toward the contact plane, and the second burst being distinctly constrained to the orbital plane.

The direction of the trends of fast ejecta quantity with EOS and total mass in our models (Figure 10) compare favorably with those found by Radice et al. (2018), with our dependence on total mass being milder. Stronger differences are found when considering the mass ratio: Radice et al. (2018) obtains a strong monotonic dependence, whereas our models yield a non-monotonic trend with changes of a factor ∼2 only. Changing the mass ratio does however result in a more broad angular distribution in our simulations, with a larger fraction of fast ejecta being launched in the orbital plane in more asymmetric binaries.

4. Implications for Kilonovae

4.1. Neutron-powered Precursors

For a given quantity of forward fast ejecta $M_{\rm n}$ that freezes out the *r*-process, which here we take to be fast ejecta with $v \geqslant 0.6c$, the peak bolometric luminosity of the ultraviolet precursor is given by (Metzger et al. 2015)

$$L_{\rm peak} = M_{\rm n}\dot{e}_n \lesssim 5 \times 10^{42}\left(\frac{M_{\rm n}}{10^{-5}\,M_\odot}\right)\ {\rm erg\ s^{-1}}, \quad (18)$$

where

$$\dot{e}_n = 3.2 \times 10^{14}(1 - 2Y_e)\ {\rm erg\ s^{-1}\ g^{-1}} \quad (19)$$

is the specific heating rate due to free neutron decay, and we have used an electron fraction $Y_e = 0.1$ to estimate an upper limit for the free neutron mass fraction in evaluating Equation (18). The corresponding time to peak emission is

$$t_{\rm peak} \simeq 0.3\ {\rm h}\left(\frac{M_{\rm n}}{10^{-5}\,M_\odot}\right)^{1/2}\left(\frac{\kappa}{1\ {\rm cm^2\ g^{-1}}}\right)^{1/2}\left(\frac{v}{0.6c}\right)^{-1/2}, \quad (20)$$

where κ is the effective gray opacity of the ejecta, the value of which can vary in the range 1–30 $\rm cm^2\,g^{-1}$, depending on the composition and ionization state of the ejecta (e.g., Tanaka et al. 2018). The fast ejecta produced in our baseline configuration, $M_{\rm n} \sim 10^{-5}\,M_\odot$ almost independent of spatial resolution, would correspond to the estimates above. Extrapolating the light curve models of Metzger et al. (2015) to lower neutron masses, one would predict that for $\sim 10^{-5}\,M_\odot$ of free neutrons, the precursor emission would peak around the *U* band (365 nm) at an AB magnitude ≈23 for a source distance of 200 Mpc. The planned wide-field ULTRASAT[6] satellite mission (Sagiv et al. 2014) is expected to reach a 5σ limiting magnitude of ∼23 for a 1 hr integration at a wavelength of 220–280 nm. ULTRASAT observations of nearby mergers (<200 Mpc) could in principle probe the neutron precursor emission given this level of fast ejecta production.

When we consider our main result of a weak dependence of $M_{\rm n}$ on spatial resolution for grid-based simulations, and the normalization of this quantity obtained in the global 3D merger simulations of Radice et al. (2018) (e.g., Figure 10), we conclude that the neutron-powered precursor luminosities and timescales in Equations (18)–(20) are likely to be an upper limit to luminosity and duration of this transient, at least as arising from the prompt dynamical ejecta. Other ways to produce fast ejecta include magnetically accelerated, neutrino-heated winds from the magnetized NS remnant (Metzger et al. 2018; Ciolfi & Kalinani 2020), outflows from accretion disks with strong initial poloidal fields (Fernández et al. 2019), jet-cocoon interactions (Gottlieb & Loeb 2020), or ablation from an early neutrino burst generated from the colliding stellar interface (Beloborodov et al. 2020). More reliable estimates of the fast ejecta from the entire merger event will therefore require realistic initial conditions and a complete physics description, including MHD and neutrino transport effects.

The freefall, head-on collision case yields $\sim 10^{-2}\,M_\odot$ of fast ejecta, with ∼10% variation with spatial resolution. Once the time to peak becomes longer than the free neutron decay time, the luminosity estimate in Equation (18) is no longer valid. Nevertheless, we expect this fact ejecta to contribute to the early kilonova signature, which should contain the imprint of much faster expansion velocities than those inferred from GW 170817 and therefore provide a distinct signature of eccentric mergers.

4.2. Nonthermal Afterglows

The dynamical ejecta is predicted to generate its own nonthermal afterglow after expanding sufficiently to interact with the interstellar medium on a timescale of years (Nakar & Piran 2011). The duration and brightness of the afterglow depend primarily on the kinetic energy distribution of the ejecta as well as on the interstellar medium density (e.g., Kathirgamaraju et al. 2019). Fast dynamical ejecta can produce an afterglow that evolves on shorter timescales of approximately months (Hotokezaka et al. 2018), and such a fast component has been proposed as a possible origin of the X-ray excess recently detected in the nonthermal GW 170817 emission (Hajela et al. 2021; Nedora et al. 2021).

Here, we focus on the implications of our resolution study for the expected kilonova afterglows from BNSs. Given that our simulations are Newtonian, we cannot produce a reliable relativistic momentum distribution. Nevertheless, we can compute the kinetic energy of all the ejecta above a given velocity, and look at its resolution dependence.

Table 1 shows the kinetic energy of all the ejecta with radial velocities greater than $0.3c$ and $0.6c$. The first velocity was found by Kathirgamaraju et al. (2019) to be the minimum value needed to obtain a detectable afterglow. Our baseline configuration yields characteristic kinetic energies $\sim 10^{49}$ erg, a factor 100 below what is needed to generate a detectable afterglow. This is likely a consequence of the underproduction of slow ejecta by our numerical experiment relative to global 3D merger simulations (Section 3.4), given that most of the kinetic energy normally resides in slower ejecta.

Despite this underproduction, we find that there is a convergence in the kinetic energy (above both velocities) to within 10% for a resolution of 16 m, similar to the convergence in mass.This is consistent with the estimates of Kyutoku et al. (2014) for the characteristic cell size at which shock breakout is properly resolved. We note however that, in contrast to the mass, relativistic material can carry a significant fraction of the total energy; hence, the lack of relativistic kinematics makes our estimates of energy dependence on resolution only suggestive. Our results nevertheless indicate that robust predictions about the kilonova afterglow from the dynamical ejecta require higher spatial resolution than used to date in global 3D merger simulations.

[6] https://www.weizmann.ac.il/ultrasat/

5. Summary

We have carried out a numerical experiment to probe the sensitivity to spatial resolution of fast ejecta ($v > 0.6c$) generation in grid-code simulations of binary NS mergers. Discrepancies in the amount of this ejecta of an order of magnitude or larger have been found in global 3D merger simulations using grid codes compared to the amounts found in SPH simulations. We implement an axisymmetric model of stellar collision in a corotating frame, including the effects of inertial forces and GW losses (Sections 2.1 and 2.2). The lower computational expense of this setup allow us to probe spatial resolutions up to 4 m, or $\sim 3 \times 10^{-4}$ of the NS radius, smaller than the finest grids used thus far in global 3D simulations of NS mergers by a factor of $\sim$20, and capturing the surface pressure scale height of the stars above within 0.1% of the stellar surface (Figure 3). Our main results are the following:

1. Our baseline configuration of two $1.4\,M_\odot$ NSs with radius 12.6 km ejects $\sim 10^{-5}\,M_\odot$ of fast ejecta, with variations in this quantity of at most a factor of $\sim$2 over a factor 140 in cell size, converging to within 10% at a spatial resolution of 20 m (Figure 9). While the absolute amount of ejecta is influenced by the approximations made in our reduced dimensionality experiment, the sensitivity to spatial resolution should be a robust outcome because of lack of strong curvature effects and a limited fraction of the ejecta moving at relativistic speeds that introduce significant length-contraction effects. We conclude that existing grid-based, global 3D hydrodynamic simulations of BNS mergers (e.g., Radice et al. 2018) are close to converging in the amount of fast ejecta, and the known discrepancy with SPH simulations is unlikely to be caused by lack in resolution. A quantity of fast of ejecta of the order of $\sim 10^{-5}\,M_\odot$ is detectable with upcoming space-based UV facilities out to $\lesssim$200 Mpc (Section 4).
2. A head-on collision at the freefall speed can eject $\sim 10^{-2}\,M_\odot$ of both fast and slow ejecta (Figure 5, Table 1). For the case in which such a collision becomes possible due to a highly eccentric merger, the corresponding kilonova signature can be distinct from that arising in a more conventional quasi-circular merger driven by GW emission. When varying the resolution by a factor of 4, we find that the total ejecta from our head-on collision models can vary non-monotonically at the $\sim$20% level.
3. Our numerical experiment reproduces the overall trends of fast ejecta generation with compactness (EOS) and total binary mass (Figure 10) when compared to the global 3D study of Radice et al. (2018). We find a non-monotonic dependence on mass ratio, which differs from that found previously. These differences can be attributed primarily to the approximations made in our experiment, particularly the reduced dimensionality and functional form of GW losses (Sections 2.1 and 2.2). While we observe production of fast ejecta in bursts in our default configuration (Figure 6), the nature of these bursts is such that ejection is primarily in the contact plane direction, in contrast to the global simulations of Radice et al. (2018) in which the second, more robust burst is confined to the equatorial plane. Additionally, our models preclude the possibility of prompt BH formation, which can occur at high total binary masses and result in reduced ejecta production relative to what we find.
4. The kinetic energy of the fast ejecta has a similar dependence on resolution than the mass. This suggests that predictions for the nonthermal kilonova afterglow require global 3D simulations with higher resolutions than those done thus far.

Four additional channels have been proposed for the production of fast ejecta: neutrino-driven outflows from magnetized NS remnants (Metzger et al. 2018; Ciolfi & Kalinani 2020), outflows from accretion disks with strong initial poloidal fields (Fernández et al. 2019), cocoon-jet interactions (Gottlieb & Loeb 2020), or ablation of stellar material by neutrinos (Beloborodov et al. 2020). A more realistic estimate of the total amount of fast ejecta produced in a binary NS merger thus requires (1) modeling the collision in general-relativistic MHD with adequate neutrino transport and with sufficient spatial resolution, and (2) use of realistic post-merger initial conditions in the case where fixed-metric codes are used. Such a calculation would provide useful information beyond the fast ejecta, and therefore is a valuable direction to pursue.

The head-on collision of NSs at the freefall speed remains a simpler problem which, when done in numerical relativity and with sufficient spatial resolution, can yield useful predictions for the ejecta components from eccentric mergers, allowing an estimate of the EM signal and nucleosynthesis contributions from these collisions.

We thank Steven Fahlman, Mario Ivanov, Sharon Morsink, and Erik Rosolowsky for helpful discussions. We also thank the anonymous referee for helpful comments that improved the paper. C.D. and R.F. acknowledge support from the Natural Sciences and Engineering Research Council of Canada (NSERC) through Discovery Grant RGPIN-2017-04286, and from the Faculty of Science at the University of Alberta. C.D. also acknowledges support from the Alberta Government via the Queen Elizabeth II Scholarship and Alberta Graduate Excellence Scholarship. B.D. M. acknowledges support from NASA (Swift Guest Investigator Program grant 80NSSC20K0909) and the National Science Foundation (grant AST-2002577). The software used in this work was in part developed by the U.S. Department of Energy (DOE) NNSA-ASC OASCR Flash Center at the University of Chicago. Data visualization was done in part using `VisIt` (Childs et al. 2012), which is supported by DOE with funding from the Advanced Simulation and Computing Program and the Scientific Discovery through Advanced Computing Program. This research was enabled in part by support provided by WestGrid (www.westgrid.ca), the Shared Hierarchical Academic Research Computing Network (SHARCNET, www.sharcnet.ca), Calcul Québec (www.calculquebec.ca), and Compute Canada (www.computecanada.ca). Computations were performed on the *Niagara* supercomputer at the SciNet HPC Consortium (Loken et al. 2010; Ponce et al. 2019). SciNet is funded by the Canada Foundation for Innovation, the Government of Ontario (Ontario Research Fund—Research Excellence), and by the University of Toronto.

Software: `FLASH` version 4.5 (Fryxell et al. 2000; Dubey et al. 2009) `matplotlib` (Hunter 2007) `NumPy` (Harris et al. 2020), `VisIt` (Childs et al. 2012).

ORCID iDs

Coleman Dean https://orcid.org/0000-0001-9364-4785
Rodrigo Fernández https://orcid.org/0000-0003-4619-339X
Brian D. Metzger https://orcid.org/0000-0002-4670-7509

References

Abbott, B. P., Abbott, R., Abbott, T. D., et al. 2017a, ApJL, 848, L12
Abbott, B. P., Abbott, R., Abbott, T. D., et al. 2017b, Natur, 551, 85
Abbott, B. P., Abbott, R., Abbott, T. D., et al. 2017c, ApJL, 848, L13
Abbott, B. P., Abbott, R., Abbott, T. D., et al. 2018, PhRvL, 121, 161101
Akmal, A., Pandharipande, V. R., & Ravenhall, D. G. 1998, PhRvC, 58, 1804
Arcavi, I. 2018, ApJL, 855, L23
Barnes, J., & Kasen, D. 2013, ApJ, 775, 18
Bauswein, A., Goriely, S., & Janka, H. T. 2013, ApJ, 773, 78
Bauswein, A., Janka, H.-T., & Oechslin, R. 2010, PRD, 82, 084043
Beloborodov, A. M., Lundman, C., & Levin, Y. 2020, ApJ, 897, 141
Blanchard, P. K., Berger, E., Fong, W., et al. 2017, ApJL, 848, L22
Bovard, L., Martin, D., Guercilena, F., et al. 2017, PhRvD, 96, 124005
Centrella, J. M., & McMillan, S. L. W. 1993, ApJ, 416, 719
Chaurasia, S. V., Dietrich, T., Johnson-McDaniel, N. K., et al. 2018, PhRvD, 98, 104005
Childs, H., Brugger, E., Whitlock, B., et al. 2012, High Performance Visualization-Enabling Extreme-Scale Scientific Insight (Berkeley, CA: Univ. California eScholarship), 357, https://escholarship.org/uc/item/69r5m58v
Ciolfi, R., & Kalinani, J. V. 2020, ApJL, 900, L35
Colella, P., & Woodward, P. R. 1984, JCP, 54, 174
Couch, S. M., Graziani, C., & Flocke, N. 2013, ApJ, 778, 181
Cowperthwaite, P. S., Berger, E., Villar, V. A., et al. 2017, ApJL, 848, L17
Dietrich, T., Ujevic, M., Tichy, W., Bernuzzi, S., & Brügmann, B. 2017, PhRvD, 95, 024029
Douchin, F., & Haensel, P. 2001, A&A, 380, 151
Drout, M. R., Piro, A. L., Shappee, B. J., et al. 2017, Sci, 358, 1570
Dubey, A., Antypas, K., Ganapathy, M. K., et al. 2009, ParC, 35, 512
Fernández, R., & Metzger, B. D. 2016, ARNPS, 66, 23
Fernández, R., Tchekhovskoy, A., Quataert, E., Foucart, F., & Kasen, D. 2019, MNRAS, 482, 3373
Fontes, C. J., Fryer, C. L., Hungerford, A. L., et al. 2015, HEDP, 16, 53
Fryxell, B., Olson, K., Ricker, P., et al. 2000, ApJS, 131, 273
Gold, R., Bernuzzi, S., Thierfelder, M., Brügmann, B., & Pretorius, F. 2012, PhRvD, 86, 121501
Goriely, S., Bauswein, A., Janka, H. T., et al. 2014, in AIP Conf. Ser. 1594, ed. S. Jeong et al. (Melville, NY: AIP), 357
Gottlieb, O., & Loeb, A. 2020, MNRAS, 493, 1753
Hajela, A., Margutti, R., Bright, J. S., et al. 2021, arXiv:2104.02070
Harris, C. R., Millman, K. J., van der Walt, S. J., et al. 2020, Natur, 585, 357
Hotokezaka, K., Kiuchi, K., Kyutoku, K., et al. 2013, PhRvD, 87, 024001
Hotokezaka, K., Kiuchi, K., Shibata, M., Nakar, E., & Piran, T. 2018, ApJ, 867, 95
Hunter, J. D. 2007, CSE, 9, 90
Ishii, A., Shigeyama, T., & Tanaka, M. 2018, ApJ, 861, 25
Just, O., Bauswein, A., Ardevol Pulpillo, R., Goriely, S., & Janka, H. T. 2015, MNRAS, 448, 541
Kasen, D., Badnell, N. R., & Barnes, J. 2013, ApJ, 774, 25
Kathirgamaraju, A., Giannios, D., & Beniamini, P. 2019, MNRAS, 487, 3914
Kellerman, T., Rezzolla, L., & Radice, D. 2010, CQGra, 27, 235016
Kiuchi, K., Kawaguchi, K., Kyutoku, K., et al. 2017, PRD, 96, 084060
Kulkarni, S. R. 2005, arXiv:astro-ph/0510256
Kyutoku, K., Ioka, K., & Shibata, M. 2014, MNRAS, 437, L6
Lehner, L., Liebling, S. L., Palenzuela, C., et al. 2016, CQGra, 33, 184002
Levan, A. J., Lyman, J. D., Tanvir, N. R., et al. 2017, ApJL, 848, L28
Li, L.-X., & Paczyński, B. 1998, ApJL, 507, L59
Lippuner, J., Fernández, R., Roberts, L. F., et al. 2017, MNRAS, 472, 904
Loken, C., Gruner, D., Groer, L., et al. 2010, JPhCS, 256, 012026
Martin, D., Perego, A., Arcones, A., et al. 2015, ApJ, 813, 2
Metzger, B. D., Bauswein, A., Goriely, S., & Kasen, D. 2015, MNRAS, 446, 1115
Metzger, B. D., Martínez-Pinedo, G., Darbha, S., et al. 2010, MNRAS, 406, 2650
Metzger, B. D., Thompson, T. A., & Quataert, E. 2018, ApJ, 856, 101
Nakar, E., & Piran, T. 2011, Natur, 478, 82
Nedora, V., Radice, D., Bernuzzi, S., et al. 2021, MNRAS, 506, 5908
Papenfort, L. J., Gold, R., & Rezzolla, L. 2018, PhRvD, 98, 104028
Peters, P. C. 1964, PhD thesis, California Institute of Technology
Ponce, M., van Zon, R., Northrup, S., et al. 2019, in PEARC '19: Proc. of the Practice and Experience in Advanced Research Computing on Rise of the Machines (Learning) (New York: Assoc. for Computing Machinery),
Porter, D. H., & Woodward, P. R. 1994, ApJS, 93, 309
Radice, D., Perego, A., Hotokezaka, K., et al. 2018, ApJ, 869, 130
Rasio, F. A., & Shapiro, S. L. 1992, ApJ, 401, 226
Read, J. S., Lackey, B. D., Owen, B. J., & Friedman, J. L. 2009, PRD, 79, 124032
Roberts, L. F., Lippuner, J., Duez, M. D., et al. 2017, MNRAS, 464, 3907
Rosswog, S. 2013, RSPTA, 371, 20120272
Ruffert, M., & Janka, H. T. 1998, A&A, 338, 535
Sagiv, I., Gal-Yam, A., Ofek, E. O., et al. 2014, AJ, 147, 79
Sekiguchi, Y., Kiuchi, K., Kyutoku, K., Shibata, M., & Taniguchi, K. 2016, PhRvD, 93, 124046
Shapiro, S. L. 1980, ApJ, 240, 246
Tanaka, M., & Hotokezaka, K. 2013, ApJ, 775, 113
Tanaka, M., Kato, D., Gaigalas, G., et al. 2018, ApJ, 852, 109
Tanaka, M., Utsumi, Y., Mazzali, P. A., et al. 2017, PASJ, 69, 102
Tanvir, N. R., Levan, A. J., González-Fernández, C., et al. 2017, ApJL, 848, L27
Wanajo, S., Sekiguchi, Y., Nishimura, N., et al. 2014, ApJL, 789, L39
Wu, M.-R., Fernández, R., Martínez-Pinedo, G., & Metzger, B. D. 2016, MNRAS, 463, 2323
Zuo, W., Bombaci, I., & Lombardo, U. 1999, PhRvC, 60, 024605